applied sciences

MDPI

Article

An Insight into a Shang Dynasty Bronze Vessel by Nuclear Techniques

Filomena Salvemini [1,*], Zeljko Pastuovic [1], Attila Stopic [1], Min-Jung Kim [2] and Sue Gatenby [2]

[1] Australia's Nuclear Science and Technology Organisation ANSTO, Lucas Heights, NSW 2234, Australia
[2] Museum of Applied Arts and Sciences, Sydney, NSW 2007, Australia
* Correspondence: filomena.salvemini@ansto.gov.au

Abstract: A bronze wine vessel attributed to 1600–1046 B.C., Shang dynasty in China, an object from the East Asian Collection of the Museum of Applied Arts and Sciences in Sydney (Australia), was studied using a non-destructive scientific analytical protocol based on the synergic combination of nuclear techniques. Gamma spectrometry, neutron-computed tomography, and proton-induced X-ray emission (PIXE) spectroscopy were applied to gain a better insight into the structural and compositional features of the artefact to prove its authenticity. Gamma spectrometry was performed to assess the risk of excessive sample activation induced by long exposure to the neutron beam and to determine the bulk elemental composition. Based on neutron-computed tomography, the porosities and the thickness of the metal wall were evaluated and found consistent with the piece-mould casting technology adopted by craftsmen during the Shang dynasty in China. Finally, PIXE spectroscopy demonstrated the use of a ternary (copper–tin-leaded) alloy and the nature of mineralisation on the surface.

Keywords: Shang dynasty; bronze vessel; nuclear techniques; non-invasive analysis

Citation: Salvemini, F.; Pastuovic, Z.; Stopic, A.; Kim, M.-J.; Gatenby, S. An Insight into a Shang Dynasty Bronze Vessel by Nuclear Techniques. *Appl. Sci.* **2023**, *13*, 1549. https://doi.org/10.3390/app13031549

Academic Editors: Maria Pia Riccardi, Daniela Di Martino and Massimiliano Clemenza

Received: 15 December 2022
Revised: 18 January 2023
Accepted: 18 January 2023
Published: 25 January 2023

1. Introduction

In the Bronze Age, the growth and maturity of a long-lasting civilisation in China were reflected in the rapid urbanisation and the creation of a new social order. Ritual cults established by the royalty and ruling aristocracy played a crucial role in maintaining social cohesion from the rise of the Erlitou culture (circa 2000 to 1600 B.C.) throughout the period of the Shang (circa 1600 to 1046 B.C.) and Zhou (circa 1046 to 221 B.C.) dynasties [1,2].

Bronze vessels were mostly commissioned by the Chinese aristocracy. They were utilised in sacrificial offerings of food and drink to gods and ancestors. These sophisticated items also served to attest the social status of the ruling class [3,4].

In the area along the Yellow River, in present-day Henan Province, where the Shang dynasty asserted its political and military power, the production of metal works flourished [4].

Although the date and origin of the Bronze Age in China are still debated, the outcomes of material and archaeological studies suggest that two basic prerequisites for copper smelting—(i) the high temperature and (ii) the control over the reducing atmosphere—evolved from the firing of pottery around 2000 B.C. [5]. Craftsmen of the Shang dynasty mastered the production of metal alloys and casting techniques. They invented a multi-stage process for casting bronze in sections of moulded clay. In the process of piece-mould casting, a clay model of an artefact was carved, and the outer clay mould was built on it. This outer shell was then cut away in sections, fired, and reassembled for casting. Depending on the shape of an object being produced, the mould assembly needed one or more cores, also of clay, in addition to the outer mould parts to provide the vessel's cavity [3,5,6].

The study of ritual bronze vessels and other skilfully manufactured bronze objects from the Shang dynasty can provide a better understanding of the early cultural and technological development in China during the Bronze Age.

At the time of writing, Chinese bronzes have been investigated using established high-sensitivity analytical techniques, thus, resulting in a wealth of information on (1) their provenance based on the lead isotope analysis [7–9], (2) the alloy composition through metallographic analysis [10–12], (3) elemental analysis by X-ray fluorescence (XRF) spectroscopy [12,13], wet chemical analysis and (electron/photon/ion) emission spectroscopy [14], (4) the manufacturing process via scanning electron microscopy (SEM), and X-ray imaging [15]. Additionally, (5) micro-Raman spectroscopy and micro-Fourier-transform infrared (FTIR) spectroscopy have been used to examine the distribution of metal phases and the extent of corrosion in Chinese bronzes [14,16]. Synchrotron radiation X-ray diffraction (XRD) spectroscopy for phase analysis, secondary ion mass spectrometry (SIMS) for Pb-isotope quantification, and inductively coupled plasma optical emission spectroscopy (ICP–OES) for the elemental analysis (As, Bi, Cr, Cu, Fe, Ni, Pb, Sb, Sn, and Zn) have been used in archaeometallurgy studies [11].

Liu and co-authors offer a comprehensive review on the evolution of studies in ancient Chinese copper-based objects in their seminal publication [12]. The scientific examination of dozens of Chinese bronze objects produced from the Erlitou culture to the Zhou dynasty and excavated in major archaeological sites is completed, and elemental and isotopic analyses on Chinese copper-based objects are greatly present in the literature. However, such investigations have been mostly based on invasive analytical procedures [5,12].

Nowadays, a non-invasive methodology for scientific investigations of precious art objects is mandatorily required by museums and other institutions collecting, restoring, and conserving art. On the contrary, most analytical tools, routinely used for the investigation of metal artefacts, are invasive, compromise the integrity of unique items, or are superficial and unable to provide information about the bulk.

The presented forensic study combines a suite of non-invasive analytical tools to characterise the structure and composition of a Shang dynasty bronze wine vessel in an attempt to prove its authenticity.

Neutron-computed tomography (n-CT) is a non-invasive technique capable of providing density-dependent spatially resolved information [17]. Structural and morphological inner features, such as the amount, distribution, and shape of defects, mainly porosity and slag inclusions, can be quantified and related to the manufacturing process [18]. For example, traces of porosity and fins where the molten metal has leaked out at a joint between mould pieces can be identified. n-CT analysis can also determine the concentration of tapped impurity and porosity, indicating the orientation of a mould when the molten alloy was poured in. Moreover, a cast-on segment may show a difference in thickness, density, or porosity from adjacent ones, or the joins may appear as a discontinuity.

In comparison to X-ray-based analytical tools with limited penetration depth in metals, neutrons offer the advantage of increased penetration power into dense materials and high sensitivity to H-based compounds. Therefore, important information on the state of conservation of an examined object can be obtained by imaging the mineralisation phases and the corrosion products deep in the bulk. The main drawback of n-CT, which is always of concern when irradiating a museum artefact, is the neutron activation of the material. Clarifying the presence of long-lived isotopes in a sample is conditional to the feasibility of any experiment inducing radioactivity when the object is part of a museum collection, and it must return to public display within an acceptable time. Therefore, we performed gamma spectrometry after a short neutron irradiation test in order to resolve any doubt about post-measurement sample activation.

Complementarily, the elemental composition of the patina and the surface corrosion products identified in several regions of interest on the vessel were investigated using accelerated ions (that have a shallow penetration depth in most solids up to 100 μm) and proton-induced X-ray emission (PIXE) spectroscopy. PIXE spectroscopy is a non-invasive, rapid, and sensitive tool for the determination of the elemental concentration of practically all elements in the periodic table, with the detection sensitivity for trace elements down to

the ppm level. After forty years of use, PIXE together with other ion beam analysis methods has developed a strong reputation for the investigation of cultural heritage objects [19–22].

2. Materials and Methods

The object of our studies is a bronze wine vessel from China, Shang dynasty, 1600–1046 B.C. The vessel has a "U" shaped body raised on tripod legs of triangular shape. It presents a loop handle issuing from an animal head. At one side of its rim, a spout is flanked by two capped finials, and a triangular flange extending to a peak is on the opposite side (Figure 1). A cast pictogram band around the body incorporates two frontal animal-like masks, the so-called *taotie*, one of the most distinctive and characteristic decorations on Shang dynasty bronze vessels. The primary attribute of a taotie is a prominent pair of eyes, often protruding in high relief. Between the eyes is a nose, often with nostrils at the base. A taotie can also include jaws and fangs, horns, ears, and eyebrows. Many versions include a split animal-like body with legs and tail, and each flank is shown in profile on either side of the mask. While following the general form described above, the appearance and specific components of taotie masks varied by period and place of origin. Other common motifs for Shang ritual bronze vessels were dragons, birds, bovine creatures, and a variety of geometric patterns. Currently, the significance of the taotie, as well as the other decorative motifs, in Shang society is unknown [1].

Figure 1. Bronze wine vessel from the Shang dynasty, made in China, Asia, 1600–1046 B.C. East Asian Collection of the Museum of Applied Arts and Sciences in Sydney, Australia.

The object is approximately 200 mm in height, 175 mm in width, and 90 mm in depth (Figure 1). It is part of the East Asian Collection of the Museum of Applied Arts and Sciences (MAAS) in Sydney, Australia.

The sample was imaged on the neutron imaging station DINGO [23] at the Australian Nuclear Science and Technology Organisation (ANSTO), Sydney.

The tomographic scan consisted of 2400 equiangularly spaced projections of 0.15° step over 360° with an exposure time of 15 s per single acquisition.

The instrument was equipped with an iKon ANDOR CCD camera with 2048 × 2048 pixels, 16 bit, and configured with an effective pixel size of 90 µm. The volumetric model was reconstructed using the Octopus code [24], then visualised and evaluated by using AVIZO 9.3 software [25].

Gamma spectrometry was performed to prevent the risk of excessive sample activation induced by long exposure to the neutron beam. The vessel was irradiated at the DINGO station with a flux of 1×10^7 neutrons per cm^2 per second with exposure to the neutron beam for 10 min. Gamma spectrometry was performed using an Ortec P-type high-purity germanium gamma detector (35% relative efficiency) connected to an Ortec digital spectrometer. Spectrum deconvolution was performed using Hyperlab software.

The PIXE measurements for bulk elemental analysis were performed at the SIBA1 end-station of the 2MV STAR accelerator of ANSTO [26]. The vessel was exposed to a low-current collimated 2.35 MeV proton beam with a flux value of ~5 nA/mm^2 and a spot size of ~3.5 mm to prevent any ion-beam-induced surface damage to the vessel. X-ray spectra were recorded for 10 min using the Vortex detector coupled to the Canberra DSP system. The elemental imaging of a flake fallen from a corroded section of the vessel was performed by PIXE microscopy using the CHIMP beamline of 6 MV SIRIUS accelerator of ANSTO [27]. PIXE microscopy experimental details for analysis of bulk solid materials in CHIMP are reported in [28]. No visual damage, usually appearing as discolouration of the irradiated area, was observed on any analysed region.

3. Past Scientific Analytical Investigations and Restoration Work

The museum's historical records report that, at the time of the acquisition of the vessel, the patina was patchy in most areas and entirely missing on the small lip where the metal was exposed. Signs of repair were visible. The repair appeared to be performed with metal and fibreglass or epoxy.

Moreover, according to the museum conservation record, there were indications that the patina was false—a mixture of paint and lacquer. In 1981, this false patina was removed by a conservation treatment using the Ardrox 20 paint stripper, left on the surface for 10 s, and then washed off with water. This treatment washed off three layers of paint and lacquer. (Lacquer; dark-green and light-green undercoat). The patina removal exposed a mended break and a white filler. A dark-green colouration covered up these crude repairs on the outside of the vase.

Additionally, the museum records state that past X-ray radiographs were performed at the Australian Atomic Energy Commission (predecessor of the ANSTO) at Lucas Heights by Mr. M. Mehrtens in 1984 (Figure 2). Mr. Mehrtens commented: "Apart from the pouring lip, the base appears to be original. It was suspected that one of the tripod legs may have been replaced, as it was at a more pronounced angle than the other two. However, the leg appears to be genuine and may have been deliberately cast that way to provide better balance as the handle is also on that side".

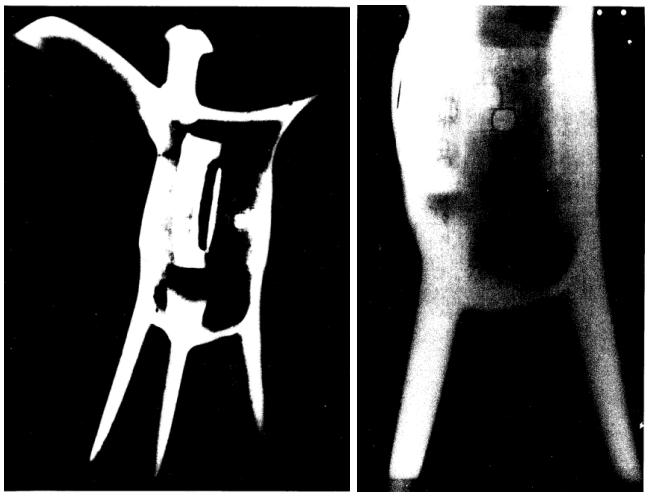

Figure 2. Previous investigation by X-ray radiography. MAAS historical record.

4. Results

4.1. Gamma Spectrometry Assurance

After a counting time of 1 week, ^{76}As, ^{122}Sb, ^{124}Sb, ^{198}Au, ^{113}Sn, ^{117}Sn, ^{140}La, and ^{24}Na typical emissions were registered. Additionally, traces of ^{110m}Ag and ^{60}Co were detected, and the overall risk of activation was considered low.

4.2. Neutron Tomography

The relevant information to emerge from the n-CT analysis of this artefact is the manufacturing method. Cast metal often displays characteristic spherical holes or porosity. As the melt cools, the solubility of the gases dissolved in the metal decreases. If the solubility limit is reached, gas will precipitate out of the melt. Because gases are much less soluble in solids than in liquids, gas build-ups ahead of the advancing freezing front increase its concentration in the reaming melt [29,30]. The 3D map of porosity extracted from the n-CT (Figure 3) shows a high distribution of spherical pores along the legs, probably the last segment to be filled where the local concentration of gases had risen. In fact, vessels with legs were cast upside down so that the legs served as inlets for pouring the alloy (https://asia.si.edu/learn/ancient-chinese-bronzes/bronze-age-casting/) (accessed on 10 January 2023) [1,3,5,6].

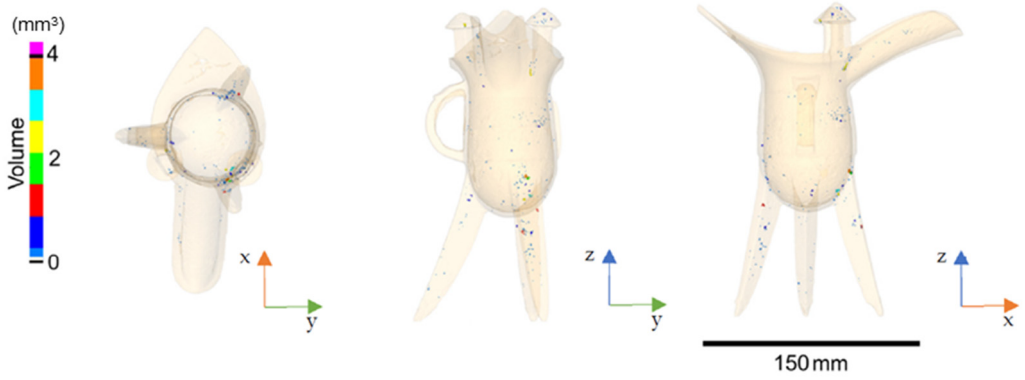

Figure 3. A 3D map of the porosities is shown in the planes xy (**a**), zy (**b**), and yx (**c**). The pores are represented as per their true size and colour-coded according to their volume, as expressed by the scale on the left. The vase is rendered with a semi-transparent surface.

Another source of porosity in casting originates from the gases that are released through the joints of the mould diffusing into the casting surface [31]. Therefore, an indication of the number and orientation of the mould components can be inferred from the distribution of tapped porosity [3]. In the vessel, porosities appear preferentially distributed in the wall of the vase along three major axes, at the correspondence of the legs, thus, suggesting the use of three pieces.

Based on the statistical analysis performed using AVIZO software [25] and reported in Table 1, the porosities, detected in small amounts in the sample, only account for 0.05% of the whole volume and feature a regular shape—an average 3D Feret shape (the Feret diameter is a one-dimensional measurement that estimates how "wide" an object is when projected by a particular angle measured on sampling in a distribution of different directions, and the 3D Feret shape is the ratio between the shortest Feret diameter and its normal Feret diameter) of 1.642 is typically indicative of a spherical particle. This suggests that pores originated earlier in solidification because gas bubbles formed later in the process typically display an irregular shape due to the physical constraints imposed by the existing dendritic network [31].

Table 1. Statistical analysis of detected porosity.

Volume			Aspect Ratio		3D Feret Shape	Equivalent Diameter	
Total	Average	Fraction	Average length	Average width		Min	Max
mm^3	mm^3	%	mm			mm	
59.257	0.225	0.05	1.091	0.626	1.642	0.335	1.994

Furthermore, cast-on segments may show a difference not only in porosity but also in the thickness of the wall [3]. A tridimensional map of the thickness of the vessel was computed on the generated surface of the n-CT reconstruction. The superficial mineralisation was virtually removed to evaluate the originally cast metal material only. Because mineralisation, porosities, and metal show a strong difference in neutron attenuation intensity, expressed as a grey value, these three components can be virtually separated through threshold segmentation. In the segmentation, each pixel in the slice images composing the n-CT stack is assigned to a label, which describes the region or material associated with the pixel (e.g., mineralisation, pores, or metal) based on its grey value. Then, the segmented components can be further manipulated and evaluated. In our case, the extracted volume of the metal was converted into a surface model composed of triangles. At each vertex of the generated metal surface, the distance along the vertex normal to the normal's intersection with the closest triangle was evaluated to create a surface scalar field of distance measure per vertex (Figure 4).

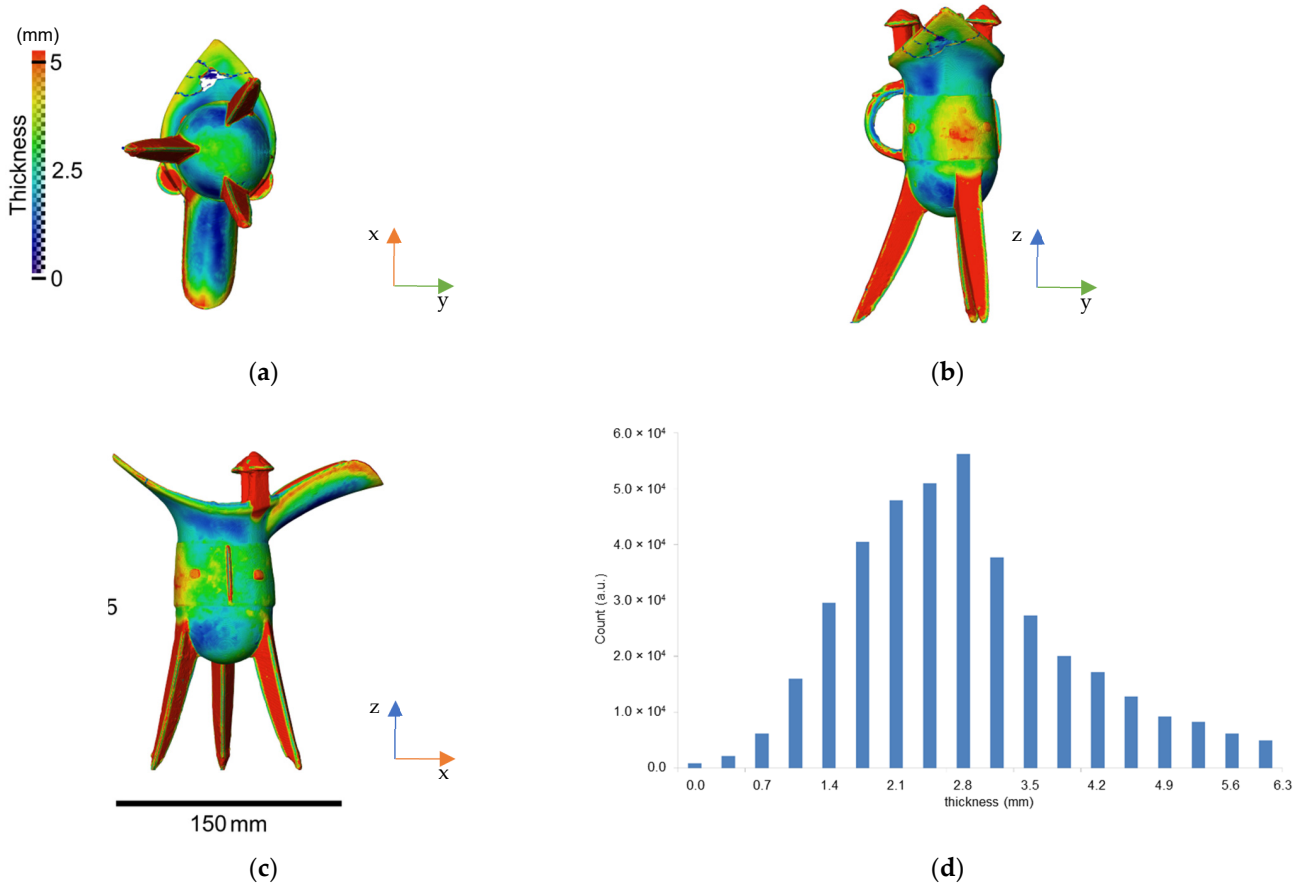

Figure 4. A 3D map of the thickness of the wall of the vase is shown in the planes xy (**a**), zy (**b**), and yx (**c**), and the frequency distribution of thickness of the wall (**d**). The volume of the vase is colour-coded according to the thickness of the material, as expressed by the scale on the top-left corner.

If the decorative elements are smoothed out and only the body of the vase is considered, some subtle variations in the thickness can be observed along the wall. Approximately, in line with the frontal leg in Figure 4b, the thickness of the wall varies, and two distinct segments can be recognised. According to the literature, three pieces are expected to be used for the casting of this portion. Although the use of such configurations is also supported by the distribution of porosities, the authenticity of the vessel neither can be conclusively confirmed nor excluded from the variation in the wall thickness alone.

A green layer of patina covers the entire surface of the artefact (Table 2) with a thickness ranging from a few hundred µm to 3 mm (Figure 5). Its composition is not uniform as it can be inferred from the attenuation coefficients. The linear attenuation coefficient $\mu_{(\lambda)}$ of the sample at the neutron wavelength λ is defined as:

$$\mu_{(\lambda)} = \sigma_{t_{(\lambda)}} \cdot \frac{\rho N_A}{M}$$

where σ_t is an element's total cross-section for neutrons of wavelength λ, ρ is the sample's density, M is its molar mass, and N_A is Avogadro's number. The total cross-section is the sum of the element's absorption and scattering cross-sections [17].

Table 2. Quantified percentage of the volume occupied by metal components, porosity, and external patina.

Component	Volume %
Vase	83.47
Porosities	0.05
Patina	16.52

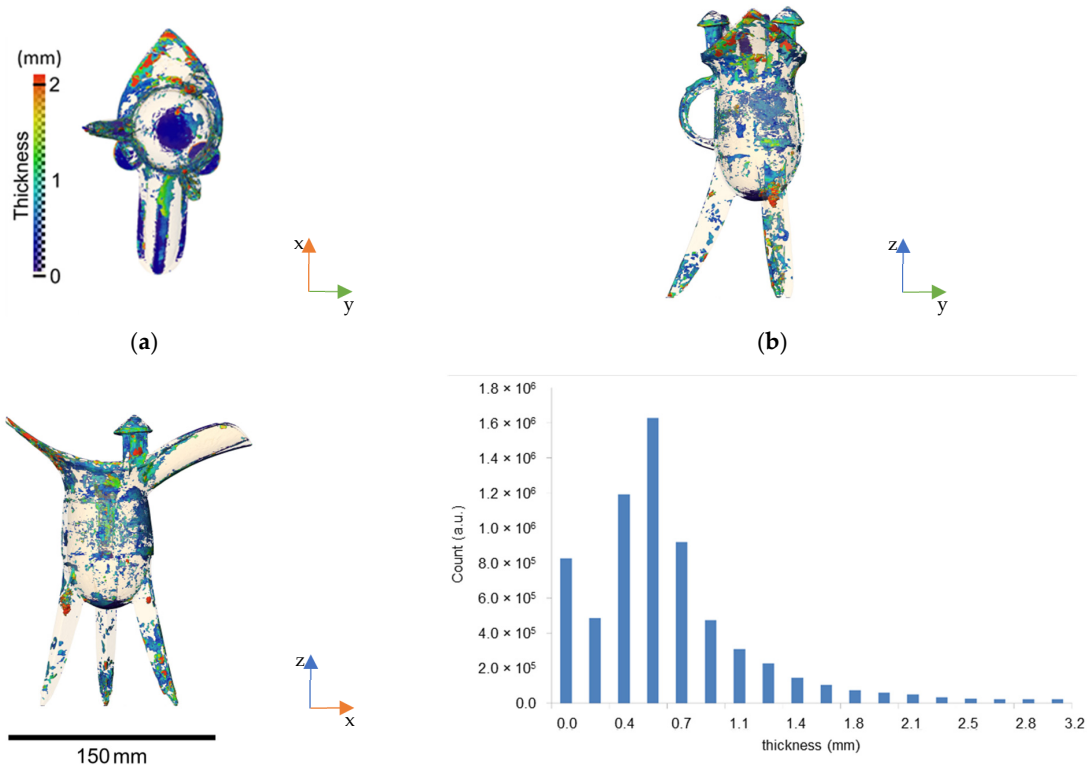

Figure 5. A 3D map of the patina thickness of the vase is shown in the planes xy (**a**), zy (**b**), and yx (**c**). The volume of the patina is colour-coded according to the thickness of the material, as expressed by the scale on the top-left corner. The vase is rendered with a semi-transparent surface. (**d**) The distribution of the thickness of the patina in the histogram shows a bimodal distribution.

μ is estimated from the measurements. The variation in μ through a selected cross-section of the vessel is shown in three different locations—one at the handle and two at the wall (Figure 6a). In the plots (Figure 6b–d), a μ value of about ~0.50 cm^{-1} can be observed consistently where the metal alloy is still well preserved. Instead, on the surface, where the patina is located, the average value is ~0.62 cm^{-1}, and ranges from 0.8 cm^{-1} to 0.4 cm^{-1}, probably because it is composed of a mixture of different copper-based compounds.

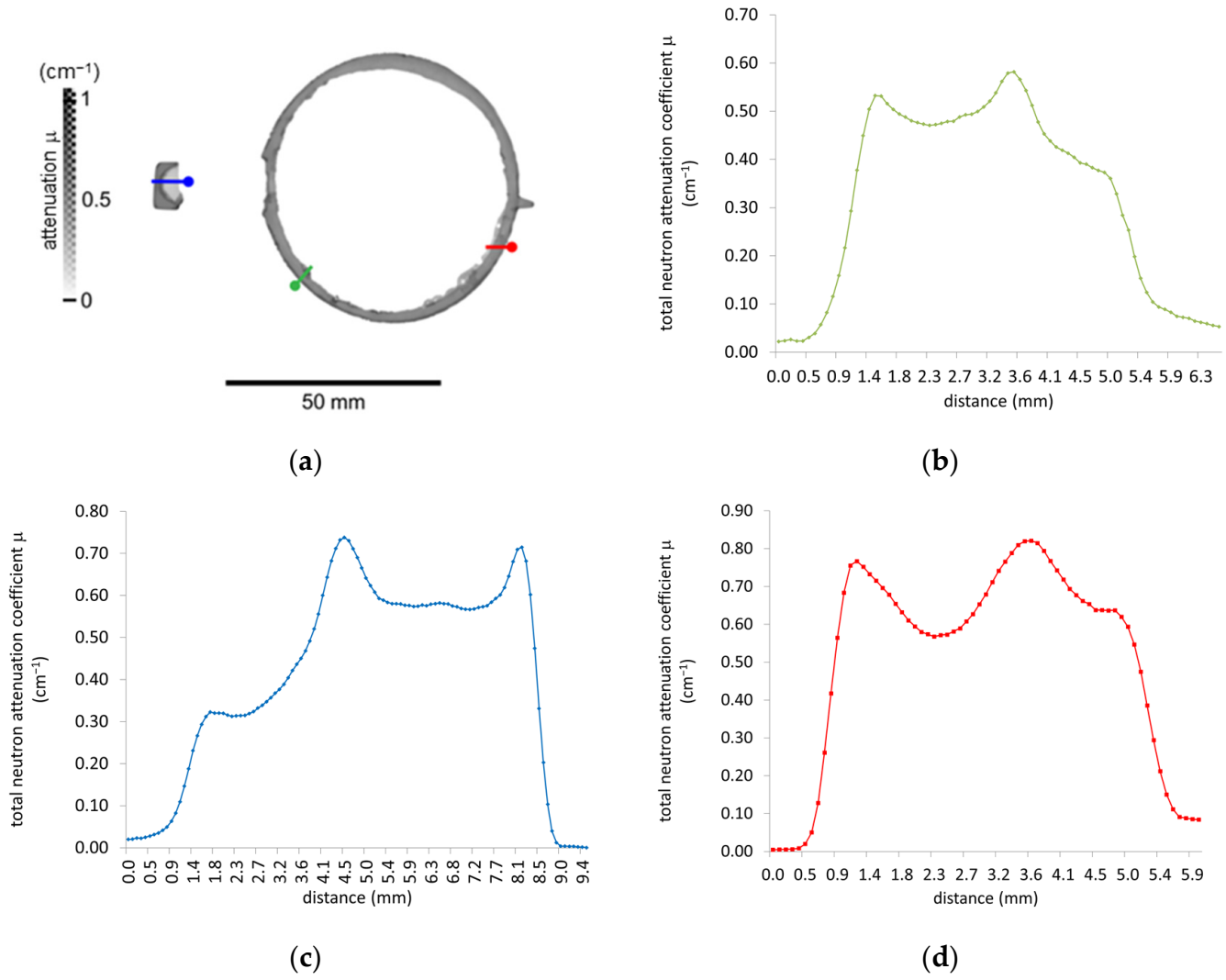

Figure 6. (**a**) An xy cross-section of the neutron tomography from the vase centre; the scale on the left side indicates the correspondence between grey tone and neutron linear attenuation coefficients experimentally imaged. (**b**–**d**) Profiles of the neutron attenuation coefficients plotted at the correspondence of the markers reported in (**a**). The same colour code is used for the profiles and the markers.

Furthermore, the n-CT demonstrates that the corrosion is not limited to the surface. Highly neutron-attenuating material can be observed in the bulk from a tomographic cross-section of the legs (Figure 7a). The attenuation profile recorded on a selected region (Figure 7b) shows that the corrosion gradually diffuses from the surface into the centre of the leg (μ values ranging between 0.6 and 1 cm^{-1}).

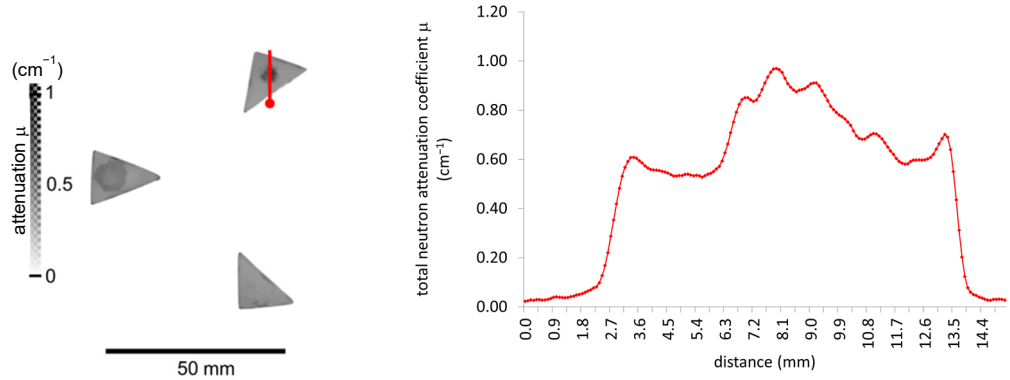

(**a**) (**b**)

Figure 7. (**a**) An xy cross-section of the neutron tomography from the legs of the object; the scale on the left side indicates the correspondence between grey tone and neutron attenuation coefficients experimentally imaged. (**b**) The profile is plotted at the correspondence of the marker reported in (**a**).

In Figure 8, the location of the metal repair is visualised. Based on the experimental attenuation coefficient (average μ of 0.27 cm^{-1}), the use of plastic or other H-based material can be excluded, while the application of a tin-based alloy is suggested. In fact, the theoretical attenuation coefficients of tin calculated at the pick of the Maxwellian distribution of the neutron flux on DINGO (1.08 Å) is around 0.2 cm^{-1}. Variation from the theoretical value can be explained by the presence of added elements such as Cu (μ of 0.87 cm^{-1}).

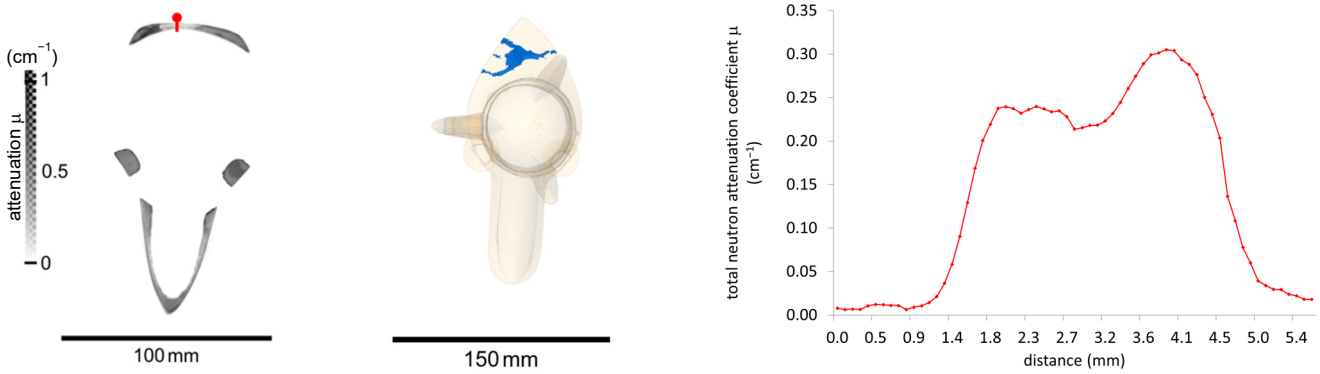

(**a**) (**b**) (**c**)

Figure 8. (**a**) An xy cross-section of the neutron tomography from the vase top; the scale on the left side indicates the correspondence between grey tone and neutron attenuation coefficients. (**b**) An xy orthogonal view of the 3D model showing the repair in blue. The vase is rendered with a semi-transparent surface. (**c**) The profile of the neutron attenuation coefficients plotted at the correspondence of the red marker reported in (**a**).

An animation showing the n-CT and the evaluations computed on the base of the 3D model are provided as Supplementary Materials (Video S1).

4.3. Particle-Induced X-ray Emission—PIXE Analysis

We investigated the elemental composition of the surface corrosion products and attempted to obtain some qualitative indications about the alloy constituents by investigating a flake (2 mm × 10 mm in size), which had fallen off from the leg position, with PIXE microscopy. Figure 9 shows elemental distribution maps 2 mm × 2 mm in size from different areas of the flake. Assuming that the positions rich in copper correspond to the main bronze material, the calculated elemental content of bronze is Cu (13.6 ± 1.5)%, Sn (71.9 ± 0.7)%, Pb (11.6 ± 0.1)%, As (1.6 ± 0.2)%, Fe (0.7 ± 0.1)%, and Ni (0.17 ± 0.02)%.

As reported in the literature [12], binary (copper–tin bronze or leaded copper) and ternary (leaded bronze) alloys were commonly employed in early dynastic China (Shang and Zhou dynasties). Chinese craftsmen were conscious of the relationship between alloy formulation and functionality; they deliberately modified the alloy with tin and lead to increase the fluidity of the melt for easier casting or to obtain the desired mechanical properties, such as hardness, colour, or toughness. However, in the investigated sample, the relative content of the alloying elements Cu, Sn, and Pb appears to be strongly affected by corrosion mechanisms such as decuprification phenomena causing enrichment in Sn. Although the exact composition of the bulk metal cannot be reliably quantified, the analysis cannot be disregarded, as it suggests the use of a ternary alloy.

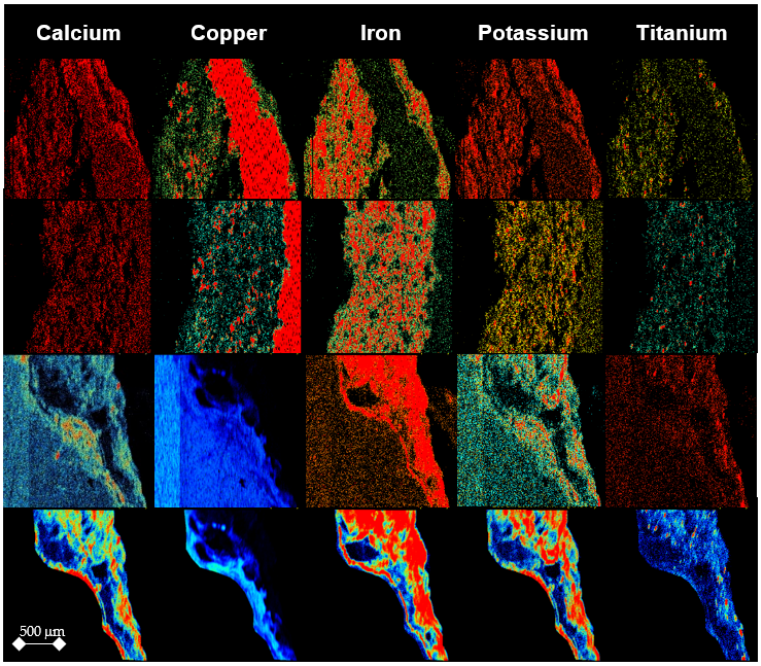

Figure 9. Elemental distributions in different areas of the fragment investigated by PIXE microscopy.

Some observations can be made about the patina. The bronze appears to be covered by a mixture of different minerals rich in iron, calcium, and potassium. The qualitative analysis of elemental distributions suggests that the iron-rich regions are intertwined with a mixture of calcium–potassium-rich regions. Areas rich in Ca, K, and Fe can be related to contaminants from the soil of the burial contest, i.e., calcite, iron oxides, potassium carbonate, or potassium oxide. Further details on the composition of the associated minerals could be potentially ascertained by complementing PIXE analysis with other non-invasive methods. For example, Mossbauer ^{119}Sn spectroscopy has been applied for the detection of corrosion products to determine the degree of oxidation on the surfaces of and in the interior of tin bronzes [32,33]. Although additional analysis will be beneficial, constraints are imposed by the possibility to move the sample and the availability of analytical techniques that are in proximity to the museum collection.

5. Discussion

The combination of different nuclear techniques—gamma spectrometry, n-CT, and PIXE—was applied to non-destructively investigate the authenticity of a Shang dynasty wine bronze vessel.

The major isotopes identified by gamma spectrometry were ^{76}As, ^{122}Sb, ^{124}Sb, ^{198}Au, ^{113}Sn, ^{117}Sn, ^{140}La, and ^{24}Na. The analysis allowed assessing the overall risk of activation that was considered low.

N-CT provided information about the bulk structural and morphological features of the vase. The evaluation of the size, shape, and distribution of porosities as well as the thickness of the metal wall appears consistent with the piece-mould casting technology adopted by craftsmen during the Shang dynasty in China. Preliminary to n-CT, Gamma spectrometry was performed to assess the risk of excessive sample activation induced by long exposure to the neutron beam.

PIXE spectroscopy was performed on a loose fragment from the surface of the artifact to determine the composition of the metal. It was found that a ternary (copper–tin-leaded) alloy was used; however, the high percentage of Sn suggests that the surface of the analysed sample is heavily affected by corrosion. n-CT showed that the entire surface of the artefact is covered by a patina with a thickness ranging from a few hundred μm to 3 mm. Because a non-invasive approach is mandatory for the investigation of museum artefacts, the exact bulk composition of the alloy could not be ascertained.

Since, to date, a direct method for dating bronze artefacts has not been developed yet, the assessment of the authenticity of such materials can be explored by gathering proof through indirect methods. In this paper, we applied a non-destructive scientific analytical protocol based on the synergy combination of nuclear techniques. The structural and compositional features were consistent with the traditional manufacture of a bronze vase of the Shang dynasty in China, thus, suggesting a genuine artefact.

Supplementary Materials: The following supporting information can be downloaded at: https://www.mdpi.com/article/10.3390/app13031549/s1, Video S1: Neutron Tomography.

Author Contributions: F.S. conceived and planned the experiments, performed the neutron tomography experiment, and evaluated the neutron tomographic data; F.S. wrote the main manuscript with input from all authors; Z.P. performed the PIXE experiment and evaluated the data; A.S. performed the gamma spectroscopy experiment and evaluated the data; S.G. and M.-J.K. contributed to sample preparation, investigated museum records, and helped supervise the study. All authors reviewed the manuscript. All authors have read and agreed to the published version of the manuscript.

Funding: This research received no external funding.

Institutional Review Board Statement: Not applicable.

Informed Consent Statement: Not applicable.

Data Availability Statement: The data presented in this study are available on request from the corresponding author.

Acknowledgments: The authors thank Vladimir Levchenko at ANSTO, Lucas Heights, NSW, Australia, for conducting the radiocarbon dating analysis. The rendering was supplied with permission by the Museum of Applied Arts and Sciences (MAAS) Powerhouse Ultimo, The Invisible Revealed exhibition: https://www.maas.museum/event/the-invisible-revealed/ (accessed on 1 January 2020).

Conflicts of Interest: The authors declare no conflict of interest.

References

1. Hohensee, N. The Metropolitan Museum of Art, Heilbrunn Timeline of Art History. Available online: https://www.metmuseum.org/toah/ (accessed on 10 January 2023).
2. Barnes, G.L. *Archaeology of East Asia: The Rise of Civilization in China, Korea and Japan*; Oxbow Books: Oxford, UK, 2015.
3. Avril, E.; Bonadies, S. Digital radioscopic examination of ancient bronze castings. In *Review of Progress in Quantitative Nondestructive Evaluation*; Springer: Berlin/Heidelberg, Germany, 1991; Volume 10B.
4. Thorp, R.L. *China in the Early Bronze Age Shang Civilization*; University of Pennsylvania Press: Philadelphia, PA, USA, 2006.
5. Linduff, K.M.; Mei, J. *Modeling Early Metallurgy: Old and New World Perspectives, in Metallurgy in Ancient Eastern Asia: How Is It Studied? Where Is the Field Headed?* SAA: Vancouver, BC, Canada, 2008.
6. Clunas, C. Art in China. Oxford History of Art. *China Rev. Int.* **1999**, *6*, 79–83.
7. Brill, R.H.; Wampler, J.M. Isotope studies of ancient lead. *Am. J. Archaeol.* **1967**, *71*, 63–77. [CrossRef]
8. Zhu, B. The mapping of geochemical provinces in China based on Pb isotopes. *J. Geochem. Explor.* **1995**, *55*, 171–181. [CrossRef]
9. Sun, W.-D.; Zhang, L.-P.; Guo, J.; Li, C.-Y.; Jiang, Y.-H.; Zartman, R.E.; Zhang, Z.-F. Origin of the mysterious Yin-Shang bronzes in China indicated by lead isotopes. *Sci. Rep.* **2016**, *6*, 23304. [CrossRef] [PubMed]

10. Carpenter, H.C.H.; Academia Sinica National Research Institute of History and Philology. *Excavation Report of Anyang, IV, Taiwan*; Preliminary Report on Chinese Bronzes; Academia Sinica National Research Institute of History and Philology: Beijing, China; Nanjing, China, 1933; pp. 677–680.
11. Scott, D.A.; Podany, J.; Considine, B.B. Ancient & Historic Metals: Conservation and Scientific Research. In *Proceedings of a Symposium on Ancient and Historic Metals Organized by the J. Paul Getty Museum and the Getty Conservation Institute, November 1991*; Getty Conservation Institute: Marina del Rey, CA, USA, 1994.
12. Liu, R.; Bray, P.; Pollard, A.; Hommel, P. Chemical analysis of ancient Chinese copper-based objects: Past, present and future. *Archaeol. Res. Asia* **2015**, *3*, 1–8. [CrossRef]
13. Song, J.; Nan, P. *Scientific Analysis of Bronzes in Western Zhou Site of Hengshui Jiangxian*; Science Press Kexue Chubanshe: Beijing, China, 2012; ISBN 9787030350039.
14. Bavarian, B.; Reiner, L.R. *Piece Mold Lost Wax & Composite Casting Techniques of the Chinese Bronze Age*; California State University: Northridge, CA, USA, 2006.
15. Meyers, P.; Holmes, L. Technical Studies of Ancient Chinese Bronzes: Some Observations. In *The Great Bronze Age of China Symposium*; Los Angeles County Museum of Art: Los Angeles, CA, USA, 1983.
16. Young, M.L.; Casadio, F.; Marvin, J.; Chase, W.T.; Dunand, D.C. An ancient Chinese bronze fragment re-examined after 50 years: Contribution from modern and traditional techniques. *Archaeometry* **2010**, *52*, 1015–1043. [CrossRef]
17. Anderson, I.; McGreevy, R.L.; Bilheux, H.Z. *Neutron Imaging and Applications. A Reference for the Imaging Community*; Springer: New York, NY, USA, 2008.
18. Salvemini, F.; White, R.; Levchenko, V.A.; Smith, A.M.; Pastuovic, Z.; Stopic, A.; Luzin, V.; Tobin, M.J.; Puskar, L.; Howard, D.; et al. Cultural Heritage Project at Australian Nuclear Science and Technology Organisation (ANSTO). In *Handbook of Cultural Heritage Analysis*; Springer International Publishing: Berlin/Heidelberg, Germany, 2022; pp. 375–441.
19. Zucchiatti, A. Ion beam analysis for the study of our cultural heritage: A short history and its milestones. *Nucl. Instrum. Methods Phys. Res. Sect. B Beam Interact. Mater. At.* **2019**, *452*, 48–54. [CrossRef]
20. Johansson, T.B.; Akselsson, R.; Johansson, S.A.E. X-ray analysis: Elemental trace analysis at the 10−12 g level. *Nucl. Instrum. Methods* **1970**, *84*, 141–143. [CrossRef]
21. Morris, W.G. PIXE: A Novel Technique for Elemental Analysis. S. A. E. Johansson and J. L. Campbell Published by John Wiley & Sons, New York (1988); 347 pages, ISBN 0471920118. *X-ray Spectrom.* **1989**, *18*, 248.
22. Nastasi, M.; Mayer, J.W.; Wang, Y. *Ion Beam Analysis*; CRC Press: Boca Raton, FL, USA, 2019.
23. Garbe, U.; Randall, T.; Hughes, C.; Davidson, G.; Pangelis, S.; Kennedy, S.J. A New Neutron Radiography/Tomography/Imaging Station DINGO at OPAL. *Phys. Procedia* **2015**, *69*, 27–32. [CrossRef]
24. Dierick, M.; Masschaele, B.; Hoorebeke, V. Octopus, a Fast and User-friendly Tomographic Reconstruction Package Developed in LabView®. *Meas. Sci. Technol.* **2004**, *15*, 1366–1370. [CrossRef]
25. Thermo Fisher Scientific. Available online: https://www.thermofisher.com/au/en/home/electron-microscopy/products/software-em-3d-vis/avizo-software.html (accessed on 10 January 2023).
26. Cohen, D.D.; Siegele, R.; Orlic, I.; Stelcer, E. Long-term accuracy and precision of PIXE and PIGE measurements for thin and thick sample analyses. *Nucl. Instrum. Methods Phys. Res. Sect. B Beam Interact. Mater. At.* **2002**, *189*, 81–85. [CrossRef]
27. Pastuovic, Z.; Button, D.; Cohen, D.; Fink, D.; Garton, D.; Hotchkis, M.; Ionescu, M.; Long, S.; Levchenko, V.; Mann, M.; et al. SIRIUS—A new 6 MV accelerator system for IBA and AMS at ANSTO. *Nucl. Instrum. Methods Phys. Res. Sect. B Beam Interact. Mater. At.* **2016**, *371*, 142–147. [CrossRef]
28. Pastuovic, Z.; Siegele, R.; Cohen, D.; Mann, M.; Ionescu, M.; Button, D.; Long, S. The new confocal heavy ion microprobe beamline at ANSTO: The first microprobe resolution tests and applications for elemental imaging and analysis. *Nucl. Instrum. Methods Phys. Res. Sect. B Beam Interact. Mater. At.* **2017**, *404*, 1–8. [CrossRef]
29. Scott, D.A. *Metallography and Microstructure of Ancient and Historical Metals*; The J. Paul Getty Trust: Los Angeles, CA, USA, 1991.
30. Habibullah, P.; Mahmood, M.A.; Anwar, Z. New casting strategy for eliminating both indigenous and exogenous gas porosity within the mould. *Codne Jnsmac* **2014**, *57*, 37–57.
31. Campbell, J. *Complete Casting Handbook: Metal Casting Processes, Metallurgy, Techniques and Design*; Elsevier: Amsterdam, The Netherlands, 2011.
32. Bandyopadhyay, D. Study of materials using Mössbauer spectroscopy. *Int. Mater. Rev.* **2006**, *51*, 171–208. [CrossRef]
33. Seeley, N.J. Mössbauer spectroscopy in archaeology. *Nature* **1975**, *254*, 479. [CrossRef]